Analysis and improvement of sound radiation performance of spherical cap radiator*

Tang Yi-Zheng(唐义政)[a], Wu Zhao-Jun(吴昭军)[b)c)], and Tang Li-Guo(汤立国)[b)c)†]

[a)] *Hangzhou Institute of Applied Acoustics, Hangzhou* 310012, *China*

[b)] *Department of Oceanography, Xiamen University, Xiamen* 361005, *China*

[c)] *Key Laboratory of Underwater Acoustic Communication and Marine Information Technology, Ministry of Education, Xiamen University, Xiamen* 361005, *China*

(Received 6 September 2009; revised manuscript received 19 November 2009)

A spherical cap radiator is one of the important parts of an underwater wide-beam imaging system. The back radiation of a traditional spherical cap radiator, which is composed of a vibrating cap and a rigid baffle, is strong and its far-field directivity function may fluctuate in big amplitude in the vicinity of the polar axis. These shortcomings complicate the processing of the reflective waves received for imaging the targets. In this study, the back radiation is weakened by adding an acoustic soft material belt between the vibrating cap and the rigid baffle. And the fluctuation mentioned above is lowered remarkably by dividing the spherical cap radiator into many annuluses and a relatively smaller spherical cap, and by controlling the phase retardations of all elements appropriately. Furthermore, the numerical experiments are carried out by the finite element method (FEM) to prove the validity of the above methods.

Keywords: spherical cap radiator, acoustic soft material, directivity

PACC: 4337, 4388

1. Introduction

Digital imaging sonar systems have broad applications in military and civil fields, such as underwater obstacle detection and avoidance, structure inspection and diver detection.[1−3] Three-dimensional (3D) imaging sonar systems have received plenty of attention in recent years because they can detect the objects accurately. Now, most of the 3D digital imaging sonars are multi-beam sonars, for example, the EchoscopeII made by CodaOctpust Group, Inc. A sonar array is often employed as the radiator in a 3D multi-beam imaging sonar system and its control circuit is complex. Compared with the multi-beam imaging sonar, a wide-beam imaging sonar is easy to design and its control circuit is simple. Theoretically, a single transducer is enough for the wide-beam imaging sonar. In order to ensure that the transmitting beam of the sonar is wide enough, the radiator is often arc-shaped. In this study, a spherical cap radiator is taken into account.

Morse studied the far-field directivity pattern and the radiation impedance of the spherical cap radiator in detail.[4] If the value of ka, where k is the wave number and a is the radius of sphere, is located in some range, for example, $20 < ka < 30$, the spherical cap radiator shows two disadvantages: one is that back radiation is strong and the other is that the directivity function may fluctuate in big amplitude in the vicinity of the polar axis. And they may complicate the processing of the reflective wave received for imaging targets. An acoustic soft material belt is added between the vibrating cap and the rigid baffle in order to weaken the back radiation. Thus, it leads to an acoustic problem with mixed boundary conditions. On the vibrating cap and the rigid baffle the radial velocity is given, and on the acoustic soft material belt the pressure is given. Up to now, the analytical solution of the above mixed boundary problem cannot be obtained. Butler employed a boundary collocation method to study the radiation from a radially vibrating polar cap mounted on an otherwise soft sphere.[5] Karnovskii and Lozovik studied the above mixed boundary problem by using the least mean square error method. However, they presented no numerical results.[6] Gerding and Thompson[7] obtained the numerical results based on the method presented by Karnovskii and Lozovik. The addition of

*Project supported by the National High Technology Research and Development Program of China (Grant No. 2006AA09Z109) and the Natural Science Foundation of Fujian Province, China (Grant No. T0750014).

†Corresponding author. E-mail: liguotang@xmu.edu.cn

© 2010 Chinese Physical Society and IOP Publishing Ltd

the acoustic soft material belt is not enough to improve the sound radiation performance of the spherical cap radiator. Something must be done to lower the big fluctuation of the directivity function in the vicinity of the polar axis. Inspired by the ultrasonic phased-array technique,[8] Tang L G and Tang Y Z[9] put forward the idea of dividing the vibrating spherical cap into many annuluses and a relatively smaller cap and controlling the phase retardations of all elements appropriately. In this study, the addition of the acoustic soft material belt and the division of the vibrating spherical cap are conducted simultaneously. And the least mean square error method is employed during the analysis. Theoretical and numerical results indicate that the sound radiation performance of the radiator is improved remarkably.

2. Sound radiation of spherical cap radiator

The directivity function of a uniformly vibrating cap with a rigid spherical baffle is[4,9]

$$D(\theta)=\frac{\left|\dfrac{1-\cos\theta_0}{\left.\dfrac{\mathrm{dh}_0^{(2)}(kr)}{\mathrm{d}(kr)}\right|_{r=a}}+\sum_{l=1}^{\infty}\dfrac{[\mathrm{P}_{l-1}(\cos\theta_0)-P_{l+1}(\cos\theta_0)]}{\left.\dfrac{\mathrm{dh}_l^{(2)}(kr)}{\mathrm{d}(kr)}\right|_{r=a}}\mathrm{e}^{\mathrm{j}(l/2)\pi}\mathrm{P}_l(\cos\theta)\right|}{\left|\dfrac{1-\cos\theta_0}{\left.\dfrac{\mathrm{dh}_0^{(2)}(kr)}{\mathrm{d}(kr)}\right|_{r=a}}+\sum_{l=1}^{\infty}\dfrac{[\mathrm{P}_{l-1}(\cos\theta_0)-\mathrm{P}_{l+1}(\cos\theta_0)]}{\left.\dfrac{\mathrm{dh}_l^{(2)}(kr)}{\mathrm{d}(kr)}\right|_{r=a}}\mathrm{e}^{\mathrm{j}(l/2)\pi}\right|}. \tag{1}$$

Figures 1 and 2 show the directivity patterns with $ka = 20.0$ and 30.0 respectively. We can find from Figs. 1 and 2 that the far-field directivity pattern of the spherical cap radiator has three main characteristics when ka is located in some range, for example, $20 < ka < 30$: (a) back radiation is strong; (b) the maximum value of the directivity function is not always located at $\theta = 0°$, for example, it is located in the vicinity of $\theta = 15°$ or 345° when $ka = 20$ and $\theta = 45°$; (c) the directivity function may fluctuate in big amplitude near the polar axis, for example, the fluctuation reaches 10dB when $ka = 30$ and $\theta = 45°$. Strong back radiation may lower the excitation efficiency and the back radiating sound reflected from underwater obstacles may interfere with the useful signal received. The big fluctuation near the polar axis complicates the processing of the reflective waves received for imaging the targets. Thus, it is necessary to take measures to lower the back radiation and the fluctuation of the directivity function near the polar axis.

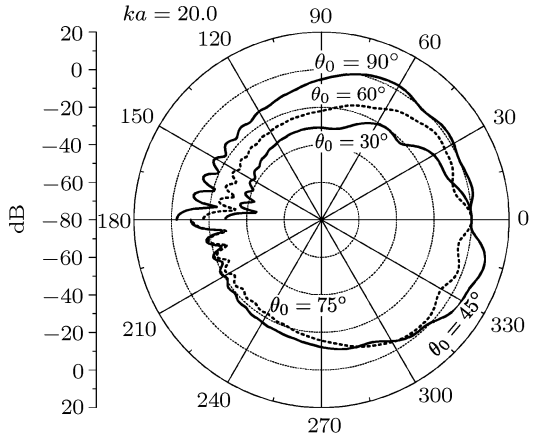


Fig. 1. Directivity patterns for the spherical cap radiator with $ka = 20.0$.

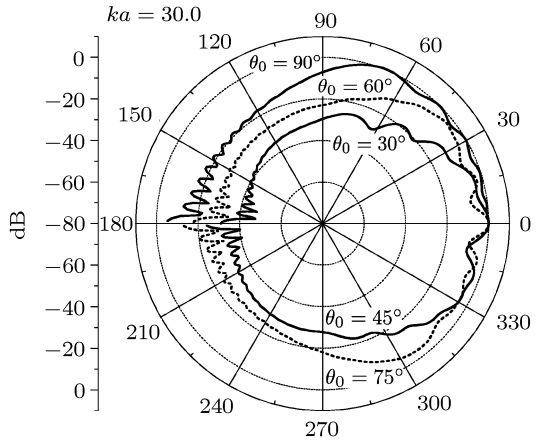


Fig. 2. Directivity patterns for the spherical cap radiator with $ka = 30.0$.

The radiation reactance and the resistance of the uniformly vibrating cap with the rigid spherical baffle, respectively, are

$$X = -\frac{S_c\rho c \sin^2\left(\frac{\theta_0}{2}\right)}{\left|\frac{\mathrm{dh}_0^{(2)}(kr)}{\mathrm{d}(kr)}\right|_{r=a}^2}\left[\mathrm{j}_0(ka)\mathrm{j}_0'(ka)+\mathrm{n}_0(ka)\mathrm{n}_0'(ka)\right] - \frac{S_c\rho c}{4\sin^2\left(\frac{\theta_0}{2}\right)}\sum_{l=1}^{\infty}\frac{\left[\mathrm{j}_l(ka)\mathrm{j}_l'(ka)+\mathrm{n}_l(ka)\mathrm{n}_l'(ka)\right]}{\left|\frac{\mathrm{dh}_l^{(2)}(kr)}{\mathrm{d}(kr)}\right|_{r=a}^2}\frac{\left[\mathrm{P}_{l-1}(\cos\theta_0)-\mathrm{P}_{l+1}(\cos\theta_0)\right]^2}{2l+1}, \quad (2)$$

and

$$R = \frac{S_c\rho c \sin^2\left(\frac{\theta_0}{2}\right)}{\left|\frac{\mathrm{dh}_0^{(2)}(kr)}{\mathrm{d}(kr)}\right|_{r=a}^2}(ka)^{-2} + \frac{S_c\rho c}{4\sin^2\left(\frac{\theta_0}{2}\right)}\sum_{l=1}^{\infty}\frac{(ka)^{-2}}{\left|\frac{\mathrm{dh}_l^{(2)}(kr)}{\mathrm{d}(kr)}\right|_{r=a}^2}\frac{\left[\mathrm{P}_{l-1}(\cos\theta_0)-\mathrm{P}_{l+1}(\cos\theta_0)\right]^2}{2l+1}, \quad (3)$$

where S_c is the area of the vibrating cap, j_l is the spherical Bessel function of order l, n_l is the spherical Neumann functions of order l, $\mathrm{h}_l^{(2)}$ is the spherical Hanker function of the second kind of order l, and P_{l-1} is the Legendre polynomial of order $l-1$.

Figures 3 and 4 show normalized radiation resistance $R/S_c\rho c$ and radiation reactance $X/S_c\rho c$ each as a function of ka and θ_0 respectively.

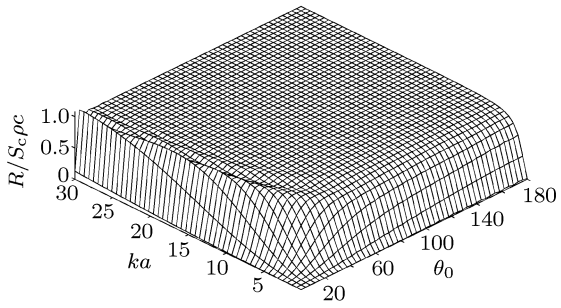


Fig. 3. Normalized radiation resistance $R/S_c\rho c$ as a function of ka and θ_0.

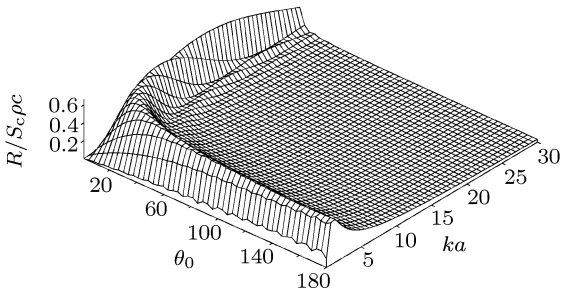


Fig. 4. Normalized reactance $X/S_c\rho c$ as a function of ka and θ_0.

It can be found from Fig. 3 that the normalized radiation resistance increases slowly with ka increasing when $0 < \theta_0 < 10°$, but when $\theta_0 > 10°$, it first increases sharply with ka increasing, and then it rises to a higher value of approximately unity. The normalized radiation reactance first increases with ka increasing, then it reaches a maximum, and for higher ka it diminishes rapidly.

3. Improvement of sound radiation performance

An acoustic soft material belt is sandwiched between the vibrating cap and the rigid baffle in order to weaken the back radiation. And it is well known that the shape and the direction of sound beam can be controlled by adjusting the retardation and the amplitude of each element of a transducer array. Inspired by the above idea, in this study it is attempted to divide the vibrating spherical cap into many annuluses and a relatively smaller spherical cap and to control the phase retardations of all elements appropriately so as to lower the big fluctuation of directivity function near the polar axis.

Figure 5 shows the spherical cap radiator after improvement, where the original vibrating cap has been divided into many annulus and a relatively smaller cap. All elements vibrate with the same amplitudes but different phases.

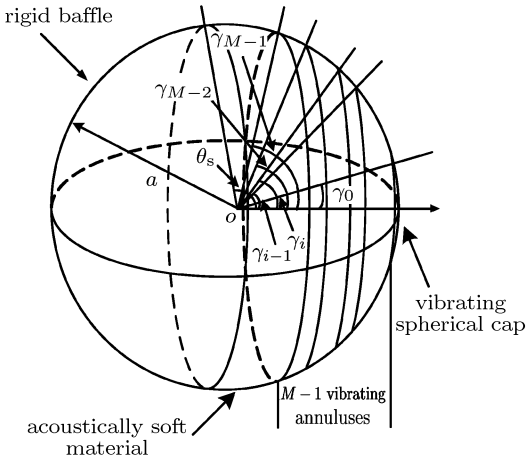


Fig. 5. Spherical cap radiator after improvement.

The sound field excited by the radiator shown in Fig. 5 is governed by

$$\nabla^2 p - \frac{1}{c^2}\frac{\partial^2 p}{\partial t^2} = 0, \tag{4}$$

and the following boundary conditions

$$v|_{r=a} = \begin{cases} v_0 \mathrm{e}^{\mathrm{j}\omega t}, & 0 \le \theta \le \gamma_0, \\ \cdots \\ v_0 \mathrm{e}^{\mathrm{j}\alpha_i}\mathrm{e}^{\mathrm{j}\omega t}, & \gamma_{i-1} \le \theta \le \gamma_i, \\ \cdots \\ v_0 \mathrm{e}^{\mathrm{j}\alpha_{M-1}}\mathrm{e}^{\mathrm{j}\omega t}, & \gamma_{M-2} \le \theta \le \gamma_{M-1}, \end{cases} \tag{5}$$

$$p|_{r=a} = 0, \gamma_{M-1} \le \theta \le \theta_s, \tag{6}$$

and

$$v|_{r=a} = 0, \quad \theta_s < \theta \le \pi, \tag{7}$$

where α_i ($i = 1,\ 2,\ \ldots,\ M-1$) are retarding phases. This is a mixed boundary problem and its analytical solution cannot be derived. The approximate methods such as the least mean square error method and boundary collocation method, are often employed to solve it. In this study, the former method is adopted. The solution of Eq. (4) under the boundary conditions Eqs. (5)–(7) can be formulated as

$$p = \sum_{n=0}^{\infty} A_n \mathrm{P}_n(\cos\theta)\mathrm{h}_n^{(2)}(kr), \tag{8}$$

where the term $\mathrm{e}^{\mathrm{j}\omega t}$ is omitted. According to the least mean square error method, the infinite series in Eq. (8) is truncated to a finite number of terms, say N, then the N unknown coefficients A_n ($n = 0, 1, \ldots, N-1$) can be determined by requiring the mean square error, i.e. the integral, over the boundary surface, of the square of the absolute value of the difference between the assumed solution at the boundary and the solution prescribed by the boundary condition, to be a minimum. The mean square error function G can be written as

$$\begin{aligned} G = &\iint_{\text{cap}} \left| \frac{\mathrm{j}}{\rho c}\sum_{n=0}^{N-1} A_n \mathrm{h}_n'(ka)\mathrm{P}_n(\cos\theta) - V_0 \right|^2 \mathrm{d}S_{\text{cap}} + \sum_{i=1}^{M-1}\beta_i \iint_{S_i} \left| \frac{\mathrm{j}}{\rho c}\sum_{n=0}^{N-1} A_n \mathrm{h}_n'(ka)\mathrm{P}_n(\cos\theta) - V_0\mathrm{e}^{\mathrm{j}\alpha_i} \right|^2 \mathrm{d}S_i \\ &+ \frac{\chi}{\rho^2 c^2}\iint_{\text{soft}} \left| \sum_{n=0}^{N-1} A_n \mathrm{h}_n(ka)\mathrm{P}_n(\cos\theta) \right|^2 \mathrm{d}S_{\text{soft}} + \lambda \iint_{\text{baffle}} \left| \frac{\mathrm{j}}{\rho c}\sum_{n=0}^{N-1} A_n \mathrm{h}_n'(ka)\mathrm{P}_n(\cos\theta) \right|^2 \mathrm{d}S_{\text{baffle}}, \end{aligned} \tag{9}$$

where β_i, χ and λ are the numerical weighting factors, h_n' denotes the derivative of h_n and the superscript (2) on the spherical Hankel function has been omitted. To minimize G, we set its derivative with respect to each of the N coefficients to be zero, i.e.

$$\frac{\partial G}{\partial A_n} = 0, \quad n = 0, 1, 2, \ldots, N-1. \tag{10}$$

It should be noted that Eq. (10) has the form of N complex linear algebraic equations in the N unknown coefficients $A_n (n = 0,\ 1, \ldots, N-1)$. We can derive from Eq. (10) that

$$\begin{aligned} &\sum_{n=0}^{N-1} A_n \mathrm{h}_n' \overline{\mathrm{h}_m'} \int_0^{\gamma_0} \mathrm{P}_n \mathrm{P}_m \sin\theta \mathrm{d}\theta + \sum_{i=1}^{M-1}\beta_i \sum_{n=0}^{N-1} A_n \mathrm{h}_n' \overline{\mathrm{h}_m'} \int_{\gamma_{i-1}}^{\gamma_i} \mathrm{P}_n \mathrm{P}_m \sin\theta \mathrm{d}\theta \\ &+ \chi \sum_{n=0}^{N-1} A_n \mathrm{h}_n \overline{\mathrm{h}_m} \int_{\gamma_{M-1}}^{\theta_S} \mathrm{P}_n \mathrm{P}_m \sin\theta \mathrm{d}\theta + \lambda \sum_{n=0}^{N-1} A_n \mathrm{h}_n' \overline{\mathrm{h}_m'} \int_{\theta_S}^{\pi} \mathrm{P}_n \mathrm{P}_m \sin\theta \mathrm{d}\theta \\ = &-\mathrm{j}\rho c V_0 \overline{\mathrm{h}_m'} \int_0^{\gamma_0} \mathrm{P}_m \sin\theta \mathrm{d}\theta - \sum_{i=1}^{M-1} j\rho c V_0 \mathrm{e}^{\mathrm{j}\alpha_i} \overline{\mathrm{h}_m'} \int_{\gamma_{i-1}}^{\gamma_i} \mathrm{P}_m \sin\theta \mathrm{d}\theta, \quad (m = 0, 1, 2, \ldots, N-1) \end{aligned} \tag{11}$$

and its detailed derivation is shown in Appendix. Setting β_i, χ and λ to be 1, we have

$$\sum_{i=0}^{M-1}\left(\sum_{n=0}^{N-1}A_n\mathrm{h}'_n\overline{\mathrm{h}'_m}\int_{\gamma_{i-1}}^{\gamma_i}\mathrm{P}_n\mathrm{P}_m\sin\theta\mathrm{d}\theta\right)+\sum_{n=0}^{N-1}A_n\mathrm{h}_n\overline{\mathrm{h}_m}\int_{\gamma_{M-1}}^{\theta_\mathrm{S}}\mathrm{P}_n\mathrm{P}_m\sin\theta\mathrm{d}\theta)$$
$$+\sum_{n=0}^{N-1}A_n\mathrm{h}'_n\overline{\mathrm{h}'_m}\int_{\theta_\mathrm{S}}^{\pi}\mathrm{P}_n\mathrm{P}_m\sin\theta\mathrm{d}\theta=\sum_{i=0}^{M-1}-j\rho cV_0\mathrm{e}^{\mathrm{j}\alpha_i}\overline{\mathrm{h}'_m}\int_{\gamma_{i-1}}^{\gamma_i}\mathrm{P}_m\sin\theta\mathrm{d}\theta,\quad(m=0,1,2,\ldots,N-1),\tag{12}$$

where $\alpha_0=0$ and $\gamma_{-1}=0$. Solving Eq. (12), we obtain the values of A_n $(n=0,1,\ldots,N-1)$. Substituting them into Eq. (8), we have the approximate expression of the pressure p. The directivity function of the radiator after improvement is

$$D_2(\theta)=\left|\frac{p(r,\theta)}{p(r,0)}\right|=\left|\frac{\sum\limits_{n=0}^{N-1}A_n\mathrm{P}_n(\cos\theta)\mathrm{h}_n(kr)}{\sum\limits_{n=0}^{N-1}A_n\mathrm{h}_n(kr)}\right|.\tag{13}$$

Apparently, the relation between the directivity function $D_2(\theta)$ and γ_i $(i=0,1,2,\ldots,M-1)$ or retarding phases α_i $(i=0,1,2,\ldots,M-1)$ is very complex. Thus, a lot of numerical experiments have been done in order to gain satisfactory results.

Considering the improvement of the spherical cap radiator with $ka=20.0$ and $\theta=45°$, we divide the vibrating cap into four annuluses and a relatively smaller cap, and the corresponding γ_i and α_i are listed in Table 1.

Table 1. γ_i and α_i corresponding to the spherical cap radiator with $ka=20.0$ and $\theta=45°$.

i	0	1	2	3	4
γ_i	27°	31.5°	36°	40.5°	45°
α_i	0	0.006π	0.028π	0.107π	0.349π

The directivity patterns can be obtained through numerical computation based on Eqs. (12) and (13). Figure 6 shows the directivity patterns of the spherical cap radiator with $ka=20.0$ and $\theta=45°$ before and after improvements, where curve 1 is for the directivity pattern before improvement, curve 2 is for the directivity pattern after division but no acoustic soft material is added, curves 3–5 are for the directivity patterns after division and adding acoustic soft material, and the values of acoustic soft material belt angle θ_s corresponding to curves 3–5 are 60°, 90° and 135°, respectively. Since the patterns are symmetric about the $0°-180°$ axis, for each pattern, only half of it is plotted. Comparing curve 2 with curve 1, we can find that the big fluctuation of the directivity function near the polar axis is weakened much after the division and the phase retardation have been introduced. Comparing curves 3–5 with curves 1 and 2, we know that the back radiation is lowered after the acoustic soft material belt has been added. And we can find from curves 3–5 that the thicker the acoustic soft material belt is, the weaker the back radiation will be, but the back radiation does not show distinct continuous decrease when θ_s is greater than 90°.

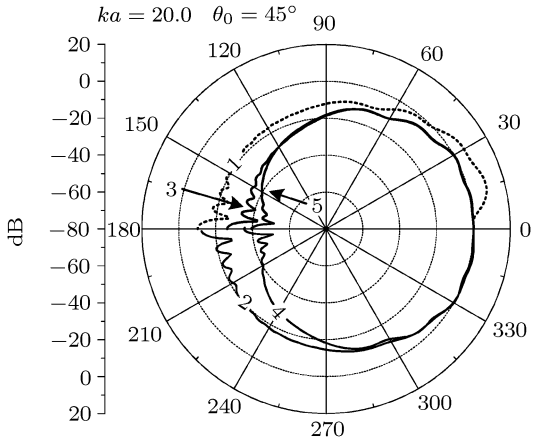


Fig. 6. Directivity patterns of the spherical cap radiator with $ka=20.0$ and $\theta=45°$ before and after improvements, where curve 1 is for the directivity pattern before improvement, curve 2 is for the directivity pattern after division but no acoustic soft material belt is added, curves 3–5 are for the directivity patterns after division and adding acoustic soft material belt, and the values of acoustic soft material belt angle θ_s corresponding to curves 3–5 are 60°, 90° and 135°, respectively.

Considering the improvement of the spherical cap radiator with $ka=30.0$ and $\theta=45°$, we divide it into five annuluses and a relatively small cap, and the corresponding γ_i and α_i are listed in Table 2.

Table 2. γ_i and α_i corresponding to the spherical cap radiator with $ka=30.0$ and $\theta=45°$.

i	0	1	2	3	4	5
γ_i	7.5°	15°	22.5°	30°	37.5°	45°
α_i	0	0.1π	0.2π	0.3π	0.4π	0.5π

Figure 7 shows the directivity patterns of the

spherical cap radiator with $ka = 30.0$ and $\theta = 45°$ before and after improvements, where curve 1 is for the directivity pattern before improvement, curve 2 is for the directivity pattern after division but no acoustic soft material is added, curves 3–5 are for the directivity pattern after division and adding acoustic soft material, and the values of acoustic soft material belt angle θ_s corresponding to curves 3–5 are 60°, 90° and 135°, respectively. We can find from Fig. 7 that the back radiation is weakened after the acoustic soft material belt has been added, and the big fluctuation of the direct function near the polar axis is lowered after the division and the phase retardation have been introduced.

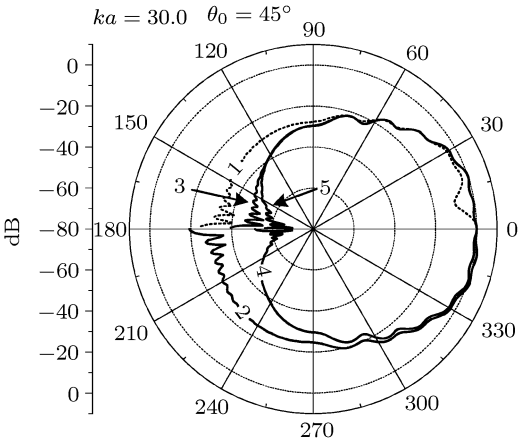


Fig. 7. Directivity patterns of the spherical cap radiator with $ka = 30.0$ and $\theta = 45°$ before and after improvements, where curve 1 is for the directivity pattern before improvement, curve 2 is for the directivity pattern after division but no acoustic soft material belt is added, curves 3–5 are for the directivity pattern after division and adding acoustic soft material belt, and the values of acoustic soft material belt angle θ_s corresponding to curves 3–5 are 60°, 90° and 135°, respectively.

4. Numerical experiment

In this section, numerical experiment is carried out to investigate the validity of the above method of improving the sound radiation performance of the spherical cap radiator. The general purpose commercial finite element software called Abaqus is used, and the implicit algorism is also employed. Figure 8 shows the axisymmetric finite element model used for the simulation. The radius of the cap, i.e. a in Fig. 8, is 0.4775 m, and the r in Fig. 8 equals $10a$. The harmonic frequency of the radiator is 10.0 kHz. The density of the water is 1000 kg/m^3, and the acoustic velocity in it is 1500 m/s. Obviously, the value of ka is about 20.0. The θ of the cap is 45°. The employed division and phase retardation are listed in Table 1.

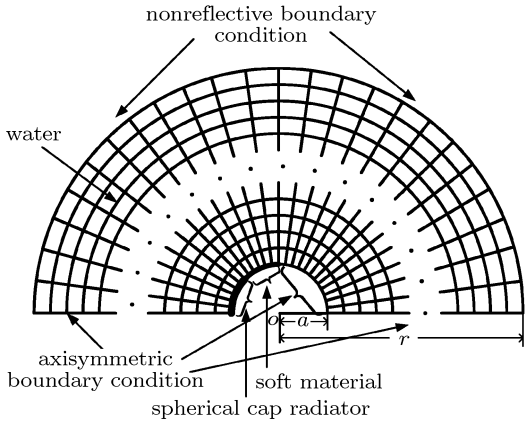


Fig. 8. Axisymmetric finite element model used for the simulation.

Figure 9 is for the simulated results by the finite element method. The curve 1 is for the directivity pattern before improvement while the curve 2 is the directivity pattern after division and adding acoustic soft material belt. The acoustic soft material belt angle θ_s corresponding to curve 2 is 90°. Comparing curve 2 with curve 1, we can find that the back radiation is weakened and the fluctuation of the far-field directivity function near the polar axis is lowered remarkably after improvement. They are consistent with the results obtained in Section 3.

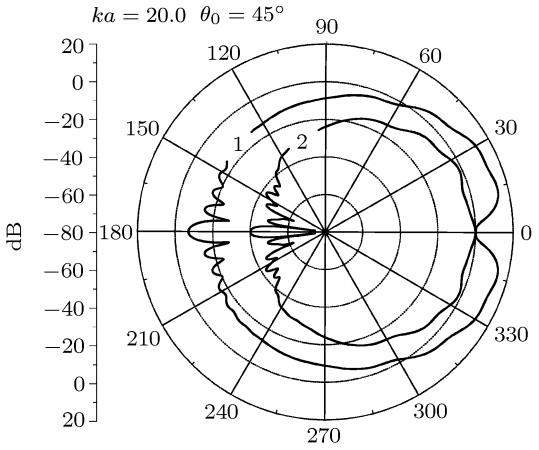


Fig. 9. Directivity patterns of the spherical cap radiator with $ka = 30.0$ and $\theta = 45°$, simulated by the finite element method (FEM), where curve 1 is the directivity pattern before improvement, curve 2 is the directivity pattern after division and adding acoustic soft material belt, and the acoustic soft material belt angle θ_s corresponding to curve 2 is 90°.

5. Conclusion

From both the theoretical and the numerical results above we know that the traditional spherical cap radiator has strong back radiation and its directivity function may fluctuate in big amplitude near the polar

axis. These shortcomings complicate the processing of the reflective waves received for imaging the targets. Two measures are taken to improve the sound radiation performance of the spherical cap radiator. One is to add an acoustic soft material belt between the vibrating cap and the rigid baffle, and the other is to divide the spherical cap radiator into many annuluses and a relatively small spherical cap and to control the phase retardations of all elements. The former is used to weaken the back radiation while the latter is used to lower the fluctuation of the directivity pattern near the polar axis. Actually, the division turns the single spherical cap radiator into an array, but its structure is still simpler than that of a multi-beam sonar. Note that the relation between the directivity function and the division mode or the retarding phases is very complex. And the optimization of the parameters corresponding to the division and phase retardation is based on a mass of numerical experiments.

Appendix A

We can obtain from Eq. (9) that

$$
\begin{aligned}
G = {} & \frac{2\pi a^2}{\rho^2 c^2}\left\{\int_0^{\gamma_0}\left\{\left[\mathrm{Re}\left(\sum_{n=0}^{N-1}A_n h'_n P_n\right)\right]^2+\left[\mathrm{Im}\left(\sum_{n=0}^{N-1}A_n h'_n P_n\right)+\rho c V_0\right]^2\right\}\sin\theta\mathrm{d}\theta\right\}\\
& +\sum_{i=1}^{M-1}\beta_i\int_{\gamma_{i-1}}^{\gamma_i}\left\{\left[\mathrm{Re}\left(\sum_{n=0}^{N-1}A_n h'_n P_n\right)\right]^2+\left[\mathrm{Im}\left(\sum_{n=0}^{N-1}A_n h'_n P_n\right)+\rho c V_0 \mathrm{e}^{\mathrm{j}\alpha_i}\right]^2\right\}\sin\theta\mathrm{d}\theta\\
& +\chi\int_{\gamma_i}^{\theta_\mathrm{s}}\sum_{n=0}^{N-1}A_n h_n P_n\overline{\sum_{n=0}^{N-1}A_n h_n P_n}\sin\theta\mathrm{d}\theta+\lambda\int_{\theta_\mathrm{s}}^{\pi}\sum_{n=0}^{N-1}A_n h_n P_n\overline{\sum_{n=0}^{N-1}A_n h_n P_n}\sin\theta\mathrm{d}\theta\\
= {} & \frac{2\pi a^2}{\rho^2 c^2}\left\{\int_0^{\gamma_0}\left[\sum_{k=0}^{N-1}\sum_{n=0}^{N-1}\overline{A_k h'_k P_k}A_n h'_n P_n\ +2\rho c V_0\mathrm{Im}\left(\sum_{n=0}^{N-1}A_n h'_n P_n\right)+\rho^2 c^2 V_0^2\right]\sin\theta\mathrm{d}\theta\right.\\
& +\sum_{i=1}^{M-1}\beta_i\int_{\gamma_{i-1}}^{\gamma_i}\left[\sum_{k=0}^{N-1}\sum_{n=0}^{N-1}\overline{A_k h'_k P_k}A_n h'_n P_n\ +2\rho c V_0\mathrm{e}^{\mathrm{j}\alpha_i}\mathrm{Im}\left(\sum_{n=0}^{N-1}A_n h' P_n\right)+\rho^2 c^2\left(V_0\mathrm{e}^{\mathrm{j}\alpha_i}\right)^2\right]\sin\theta\mathrm{d}\theta\\
& \left.+\chi\int_{\gamma_i}^{\theta_\mathrm{s}}\sum_{k=0}^{N-1}\sum_{n=0}^{N-1}\overline{A_k h'_k P_k}A_n h'_n P_n\sin\theta\mathrm{d}\theta+\lambda\int_{\theta_\mathrm{s}}^{\pi}\sum_{k=0}^{N-1}\sum_{n=0}^{N-1}\overline{A_k h'_k P_k}A_n h'_n P_n\sin\theta\mathrm{d}\theta\right\}. \qquad \text{(A1)}
\end{aligned}
$$

And we have

$$
\begin{aligned}
& \partial\left(\int_a^b\sum_{k=0}^{N-1}\sum_{n=0}^{N-1}\overline{A_k h'_k P_k}A_n h'_n P_n\sin\theta\mathrm{d}\theta\right)\Big/\partial\,\mathrm{Re}\,(A_m)\\
= {} & \partial\left[\int_a^b\sum_{\substack{n=0\\n\neq m}}^{N-1}\overline{A_m h'_m P_m}A_n h'_n P_n\sin\theta\mathrm{d}\theta+\int_a^b\sum_{\substack{n=0\\n\neq m}}^{N-1}\overline{A_n h'_n P_n}A_m h'_m P_m\sin\theta\mathrm{d}\theta\right.\\
& \left.+|A_m|^2|h_m|^2\int_a^b P_m^2\sin\theta\mathrm{d}\theta\right]\Big/\partial\,\mathrm{Re}\,(A_m)\\
= {} & \partial\left[\sum_{\substack{n=0\\n\neq m}}^{N-1}\left(\overline{A_m h'_m}A_n h'_n+\overline{A_n h'_n}A_m h'_m\right)\int_a^b P_m P_n\sin\theta\mathrm{d}\theta+|A_m|^2|h_m|^2\int_a^b P_m^2\sin\theta\mathrm{d}\theta\right]\Big/\partial\,\mathrm{Re}\,(A_m)\\
= {} & \sum_{\substack{n=0\\n\neq m}}^{N-1}2\frac{\partial\,\mathrm{Re}\left(\bar{A}_m\bar{h'}_m A_n h'_n\right)}{\partial\,\mathrm{Re}\,(A_m)}\int_a^b P_m P_n\sin\theta\mathrm{d}\theta+2\,\mathrm{Re}\,(A_m)|h_m|^2\int_a^b P_m^2\sin\theta\mathrm{d}\theta
\end{aligned}
$$

$$= \sum_{\substack{n=0 \\ n\neq m}}^{N-1} 2\,\mathrm{Re}\left(\bar{h'}_m A_n h'_n\right) \int_a^b P_m P_n \sin\theta \mathrm{d}\theta + 2\,\mathrm{Re}\left(A_m\right)|h_m|^2 \int_a^b P_m^2 \sin\theta \mathrm{d}\theta$$

$$= 2\,\mathrm{Re} \sum_{n=0}^{N-1} \left(A_n h'_n \overline{h}'_m\right) \int_a^b P_m P_n \sin\theta \mathrm{d}\theta. \tag{A2}$$

Through the derivation similar to the above, we obtain

$$\partial \left(\int_a^b \sum_{k=0}^{N-1} \sum_{n=0}^{N-1} \overline{A_k h'_k P_k} A_n h'_n P_n \sin\theta \mathrm{d}\theta \right) \Big/ \partial\,\mathrm{Im}\left(A_m\right)$$

$$= 2\,\mathrm{Im} \sum_{n=0}^{N-1} \left(A_n h'_n \overline{h}'_m\right) \int_a^b P_m P_n \sin\theta \mathrm{d}\theta. \tag{A3}$$

And it is easy to obtain

$$\partial \left[\int_a^b 2\rho c V_0\,\mathrm{Im} \left(\sum_{n=0}^{N-1} A_n h'_n P_n \right) \sin\theta \mathrm{d}\theta \right] \Big/ \partial\,\mathrm{Re}\left(A_m\right)$$

$$= 2\rho c V_0\,\mathrm{Im}\left(h'_m\right) \int_a^b P_m \sin\theta \mathrm{d}\theta, \tag{A4}$$

and

$$\partial \left[\int_a^b 2\rho c V_0\,\mathrm{Im} \left(\sum_{n=0}^{N-1} A_n h'_n P_n \right) \sin\theta \mathrm{d}\theta \right] \Big/ \partial\,\mathrm{Im}\left(A_m\right)$$

$$= 2\rho c V_0\,\mathrm{Re}\left(h'_m\right) \int_a^b P_m \sin\theta \mathrm{d}\theta. \tag{A5}$$

Then we can obtain from $\partial G/\partial\,\mathrm{Re}(A_m) = 0$, $(m = 0, 1, 2, \ldots, N-1)$ that

$$\sum_{n=0}^{N-1} \mathrm{Re}\left(A_n h'_n \overline{h'_m}\right) \int_0^{\gamma_0} P_n P_m \sin\theta \mathrm{d}\theta + \sum_{i=1}^{M-1} \beta_i \sum_{n=0}^{N-1} \mathrm{Re}\left(A_n h'_n \overline{h'_m}\right) \int_{\gamma_{i-1}}^{\gamma_i} P_n P_m \sin\theta \mathrm{d}\theta$$
$$+ \chi \sum_{n=0}^{N-1} \mathrm{Re}\left(A_n h_n \overline{h_m}\right) \int_{\gamma_{M-1}}^{\theta_s} P_n P_m \sin\theta \mathrm{d}\theta + \lambda \sum_{n=0}^{N-1} \mathrm{Re}\left(A_n h'_n \overline{h'_m}\right) \int_{\theta_s}^{\pi} P_n P_m \sin\theta \mathrm{d}\theta$$
$$= -\rho c V_0\,\mathrm{Im}\left(\overline{h'_m}\right) \int_0^{\gamma_0} P_m \sin\theta \mathrm{d}\theta - \sum_{i=1}^{M-1} \rho c V_0 \mathrm{e}^{\mathrm{j}\alpha_i}\,\mathrm{Im}\left(\overline{h'_m}\right) \int_{\gamma_{i-1}}^{\gamma_i} P_m \sin\theta \mathrm{d}\theta, \quad (m = 0, 1, 2, \ldots, N-1). \tag{A6}$$

Similarly, we can obtain from $\partial G/\partial \mathrm{Im}(A_m) = 0, (m = 0, 1, 2, \ldots, N-1)$ that

$$\sum_{n=0}^{N-1} \mathrm{Im}\left(A_n h'_n \overline{h'_m}\right) \int_0^{\gamma_0} P_n P_m \sin\theta \mathrm{d}\theta + \sum_{i=1}^{M-1} \beta_i \sum_{n=0}^{N-1} \mathrm{Im}\left(A_n h'_n \overline{h'_m}\right) \int_{\gamma_{i-1}}^{\gamma_i} P_n P_m \sin\theta \mathrm{d}\theta$$
$$+ \chi \sum_{n=0}^{N-1} \mathrm{Im}\left(A_n h_n \overline{h_m}\right) \int_{\gamma_{M-1}}^{\theta_s} P_n P_m \sin\theta \mathrm{d}\theta + \lambda \sum_{n=0}^{N-1} \mathrm{Im}\left(A_n h'_n \overline{h'_m}\right) \int_{\theta_s}^{\pi} P_n P_m \sin\theta \mathrm{d}\theta$$
$$= -\rho c V_0\,\mathrm{Re}\left(\overline{h'_m}\right) \int_0^{\gamma_0} P_m \sin\theta \mathrm{d}\theta - \sum_{i=1}^{M-1} \rho c V_0 \mathrm{e}^{\mathrm{j}\alpha_i}\,\mathrm{Re}\left(\overline{h'_m}\right) \int_{\gamma_{i-1}}^{\gamma_i} P_m \sin\theta \mathrm{d}\theta, \quad (m = 0, 1, 2, \ldots, N-1). \tag{A7}$$

It is easy to be obtained from Eqs. (A6) and (A7) that

$$\sum_{n=0}^{N-1} A_n h'_n \overline{h'_m} \int_0^{\gamma_0} P_n P_m \sin\theta \mathrm{d}\theta + \sum_{i=1}^{M-1} \beta_i \sum_{n=0}^{N-1} A_n h'_n \overline{h'_m} \int_{\gamma_{i-1}}^{\gamma_i} P_n P_m \sin\theta \mathrm{d}\theta$$
$$+ \chi \sum_{n=0}^{N-1} A_n h_n \overline{h_m} \int_{\gamma_{M-1}}^{\theta_s} P_n P_m \sin\theta \mathrm{d}\theta + \lambda \sum_{n=0}^{N-1} A_n h'_n \overline{h'_m} \int_{\theta_s}^{\pi} P_n P_m \sin\theta \mathrm{d}\theta$$
$$= -\mathrm{j}\rho c V_0 \overline{h'_m} \int_0^{\gamma_0} P_m \sin\theta \mathrm{d}\theta - \sum_{i=1}^{M-1} \mathrm{j}\rho c V_0 \mathrm{e}^{\mathrm{j}\alpha_i} \overline{h'_m} \int_{\gamma_{i-1}}^{\gamma_i} P_m \sin\theta \mathrm{d}\theta \quad (m = 0, 1, 2, \ldots, N-1). \tag{A8}$$

Equation (A8) is just Eq. (15) in Section 3.

References

[1] Gross P and Andrew P 2007 *Proc. IEEE OCEANS* (Vancouver, Canada) p1

[2] Zhao S, Anvar A and Lu T F 2008 *Proc. ICIEA* (Singapore) p1906

[3] Rose C S, Stoner A W and Matteson K 2005 *Fish. Res.* **76** 291

[4] Morse P M and Ingard K U 1986 *Theoretical Acoustics* (New York: McGraw-Hill) 332

[5] Butter J L 1970 *J. Acoust Soc. Am.* **48** 325

[6] Karnovskii M I and Lozovik V G 1965 *Sov. Phys. Acoust.* **11** 147

[7] Gerding G C and Thompson W 1977 *J. Acoust. Soc. Am.* **61** 313

[8] Lu M Z, Wang M X and Shi Y 2001 *Acta. Phys. Sin.* **50** 347 (in Chinese)

[9] Tang L G and Tang Y Z 2008 *Prog. Nat. Sci.* **18** 345 (in Chinese)